The Mutational Landscape of Cancer's Vulnerability to Ionizing Radiation

Priyanka Gopal[1], Brian D. Yard[2], Aaron Petty[2], Jessica C. Lal[2], Titas K. Bera[1], Trung Q. Hoang[1], Alexandru D. Buhimschi[1], and Mohamed E. Abazeed[1,3]

ABSTRACT

Purpose: Large-scale sequencing efforts have established that cancer-associated genetic alterations are highly diverse, posing a challenge to the identification of variants that regulate complex phenotypes like radiation sensitivity. The impact of the vast majority of rare or common genetic variants on the sensitivity of cancers to radiotherapy remains largely unknown.

Experimental Design: We developed a scalable gene editing and irradiation platform to assess the role of categories of variants in cells. Variants were prioritized on the basis of genotype–phenotype associations from a previously completed large-scale cancer cell line radiation profiling study. Altogether, 488 alleles (396 unique single-nucleotide variants) from 92 genes were generated and profiled in an immortalized lung cell line, BEAS-2B. We validated our results in other cell lines (TRT-HU1 and NCI-H520), *in vivo* via the use of both cell line and patient-derived murine xenografts, and in clinical cohorts.

Results: We show that resistance to radiation is characterized by substantial inter- and intra-gene allelic variation. Some genes (e.g., *KEAP1*) demonstrated significant intragenic allelic variation in the magnitude of conferred resistance and other genes (e.g., *CTNNB1*) displayed both resistance and sensitivity in a protein domain-dependent manner. We combined results from our platform with gene expression and metabolite features and identified the upregulation of amino acid transporters that facilitate oxidative reductive capacity and cell-cycle deregulation as key regulators of radiation sensitivity.

Conclusions: Our results reveal new insights into the genetic determinants of tumor sensitivity to radiotherapy and nominate a multitude of cancer mutations that are predicted to impact treatment efficacy.

Introduction

Radiotherapy is an integral component of cancer therapy, with considerable contributions to the curative and palliative management of patients (1). However, while drug treatments for cancer are increasingly informed by genetic data, radiotherapy continues to be delivered without accounting for the considerable genetic variation across tumors (2). Variation implies that generic treatment strategies optimized using decades of population data can lead to significant under- or overtreatment of individual patients (3). This imprecision limits radiotherapeutic efficacy and could lead to the unnecessary irradiation of organs.

The genetic features that regulate the sensitivity of cancers to ionizing radiation remain largely unknown (4). Phenotypic evaluation from human data have established some associations between SNPs or somatic variants and clinical outcomes (5, 6). Functional assays that test genetic alterations for gene activity have been generally useful in validating some genetic associations (7). In the radiation sciences, however, these efforts have historically focused on individual genes or cellular functions (e.g., DNA double-strand break repair; refs. 8, 9). However, the cellular response to radiation represents a complex phenotype with significant locus heterogeneity (10). Therefore, it is evident that the efforts to date identify a very limited set of the potential genetic alterations that could regulate the sensitivity of cancers to these treatments.

The identification of functionally relevant cancer variants remains a challenge because tumor genetic alterations can be highly diverse and complex (11). Although mutations in oncogenes often display mutational hot spots that lead to increased activity, specific variants in these hotspots can have a range of activity (12). Similarly, variants in genes with loss-of-function (LOF) alterations usually comprise a mixture of neutral or functionally consequential mutations that are scattered over the length of a gene, complicating variant interpretation. Computational (13, 14) and functional genomic (15–17) approaches have been devised to ameliorate these challenges. However, these methods largely predict the impact of variants on gene function rather than test functional variants for individual phenotypic outputs. They also reduce complex statistical and phenome (e.g., gene expression) associations to low dimension categorical bins (drivers versus passengers) or univariate scales. Because it is likely that the relationships between complex phenotypes and genetic parameters are both nonlinear and non-monotonic (18, 19), the means to unambiguously predict the impact of a common or rare cancer variant on complex phenotypes like radiation sensitivity are currently very limited.

To address these collective limitations, we conducted a systematic arrayed profiling effort to identify gene variants that alter the cellular sensitivity to ionizing radiation.

[1]Department of Radiation Oncology, Feinberg School of Medicine, Northwestern University, Chicago, Illinois. [2]Department of Translational Hematology Oncology Research, Cleveland Clinic, Cleveland, Ohio. [3]Robert H. Lurie Comprehensive Cancer Center, Northwestern University, Chicago, Illinois.

P. Gopal, B.D. Yard, and A. Petty contributed equally to this article.

Corresponding Author: Mohamed E. Abazeed, Feinberg School of Medicine, Northwestern University, 303 E. Superior St/Lurie 7-115, Chicago, IL 60611. Phone: 312-926-2520; Fax: 312-926-6524; E-mail: mabazeed@northwestern.edu

Clin Cancer Res 2022;28:5343–58

doi: 10.1158/1078-0432.CCR-22-1914

Translational Relevance

Efforts to nominate and translate biomarker-guided radiotherapy into clinical practice have had limited success to date. We developed and integrated *in silico* and experimental profiling platforms designed to identify new genetic biomarkers of radiation sensitivity. We found that tumor radiation sensitivity represents a complex phenotype that is characterized by significant inter- and intra-gene allelic variation. We also found that that although cancer genomes reflect tissue-specific variant tendencies, genetic variants that alter radiation sensitivity can confer phenotypic effects across several tissue types. The large-scale culling of large genomic datasets for variants that regulate radiation sensitivity and the validation of these features as predictive diagnostics and therapeutic targets in preclinical model systems and clinical cohorts represents an important milestone in the radiation sciences.

Materials and Methods

Cell culture

Adenovirus-12 SV40 hybrid transformed immortalized upper airway bronchial epithelial cells (BEAS-2B) were grown in advanced DMEM-F12 media (ThermoFisher, MA) supplemented with 1% FBS, 100 U/mL penicillin, 100 μg/mL of streptomycin, 292 μg/mL L-Glutamine and 1% HEPES. hTERT-immortalized human urothelial (TRT-HU1) cell line was grown in DMEM media (ThermoFisher, MA) supplemented with 10% FBS, 100 U/mL penicillin, 100 μg/mL of streptomycin, and 292 μg/mL L-Glutamine. Cancer cell lines NCI-H520 and HCC15 were authenticated per the cell lines from the Cancer Cell Line Encyclopedia (CCLE) protocol and grown in RPMI (ThermoFisher, MA) supplemented with 10% FBS (ThermoFisher, MA), 100 U/mL penicillin, 100 μg/mL of streptomycin, 292 μg/mL L-Glutamine (Corning, NY). All cultures were maintained at 37°C in a humidified 5% CO_2 atmosphere and tested to ensure the absence of *Mycoplasma*.

Plasmids

Variant-expressing lentiviral plasmids were generated in three steps: PCR, *in vitro* recombination, and transformation. Briefly, gene open reading frames (ORF) were PCR amplified by using primers that incorporate the desired mutant. Fragments were then transferred directly to the destination vectors pLX306 and/or pLX307 by LR reaction (Invitrogen, MA) and the constructs were transformed into competent cells. The discontinuity at the mutation site was repaired by endogenous bacterial repair mechanisms. After viral infection [multiplicity of infection (MOI) > 0.8], BEAS-2B cells were selected in the presence of 1 μg/mL puromycin.

Exon-intron junctional CRISPR (*j*-CRISPR). plentiCRISPRv2 plasmid (Addgene, Plasmid #83480), which contains the Cas9 coding sequence and a cloning site for single-guide RNA (sgRNA), was digested with BsmBI. Two complementary oligonucleotides with two 4-bp overhang sequences were annealed and ligated into digested pLentiCRISPRv2. sgRNAs were designed with the Synthego CRISPR web design tool (https://www.synthego.com/products/bioinformatics/crispr-design-tool/). After viral infection, BEAS-2B cells were selected in the presence of 5 μg/mL blasticidin (ThermoFisher, MA). Monoclonal cells were generated from a polyclonal pool of transduced stable cells by limited dilution. Genomic DNA from monoclonal or polyclonal cell lines was extracted using the QIAamp DNA Mini Kit (Qiagen, MD) following the manufacturer's instructions. PCR was performed with primers that flank the region(s) of interest to amplify the target sequences. PCR products were purified using the QIAquick Gel Extraction Kit (Qiagen, MD) and sequenced by the Sanger method. Sequence chromatograms comprising mixed spectra were analyzed using the Unipro UGENE software.

Genetic addback

Wild-type and variant containing ORFs of *KEAP1* and *TP53BP1* were cloned into pLX306 and pLX307, respectively, and integrated into the respective *j*-CRISPR modified or non-target control (NTC) BEAS-2B cell lines. After viral infection (MOI > 0.8), cells were selected in the presence of 1 μg/mL puromycin.

Antibodies and reagents

Anti-KEAP1 (clone D6B12, #8047, 1:1,000), anti–β-actin (clone 13E5, #4970, 1:4,000), anti-LKB1 (clone D60C5, #3047, 1:1,000), anti-Vinculin (#4650, 1:4,000), anti-TP53BP1(#4937, 1:1,000), anti-βcatenin (clone D10A8, #25362, 1:2,000), anti-phospho-p44/42 MAPK (#9101, 1:3,000), anti-phospho-MEK1/2 (clone 41G9, #9154, 1:1,000 dilution), anti-xCT/SLC7A11 (clone D2M7A, #12691, 1:1,000) were from Cell Signaling Technology, MA. Anti-NRAS antibody (#ab77392) was from Abcam, MA. Erastin (#17754) was from Cayman Chemical. Sotorasib (#HY-114277) used *ex vivo* was from MedChemExpress.

High-content radiation platform

Cells were plated using a Multidrop Combi liquid handler (ThermoFisher, MA) in at least quadruplicate wells at two distinct cell densities (150 and 200 cells/well) in white-walled 96-well plates (Corning, NY). At 7 to 9 days postirradiation, media was aspirated and 45 μL CellTiter-Glo reagent (50% solution in PBS; Promega, WI) was added to each well. Relative luminescence units were measured using a Synergy HTX or LX (Biotek, VT) luminescence plate reader. The luminescence signal was plotted as a function of cell density and a cell density within the linear range for luminescence (or growth) was selected to generate integral survival for each cell line (20). Cells were treated with γ-radiation delivered at 0.92 Gy/min with a ^{137}Cs source using a GammaCell 40 Exactor (Best Theratronics; Ontario, Canada) or using a XRad 2000, X-ray irradiator delivered at 0.525 Gy/min (Rad Source, GA). For quality assurance, thermoluminescent dosimeters were used to verify correct dose administration.

Radiation survival and synergy

The AUC was estimated using trapezoidal approximation. Values representing radiation doses 0, 2, 4, and 6 Gy were used to generate an AUC value for each variant or vector control. The survival values for each trapezoid were multiplied by the dose interval, $[f(X_1)+f(X_2)/2] \times \Delta X$ and summed. The survival values were re-scaled by $\log 2 \times (\frac{\text{Variant (AUC)}}{\text{Vector (AUC)}})$ within plate per run. The degree of combination synergy was quantified by comparing the observed combination response against the expected response, calculated using a reference model that assumes no interaction between the two therapies. SynergyFinder Plus was used to estimate the degree of synergy for radiation and drug combination studies (21).

Clonogenic survival

Cells were plated at appropriate dilutions, irradiated and incubated for 8 to 9 days for colony formation. Colonies were fixed using methanol or 1% formaldehyde and stained using 0.5% (w/v) crystal violet in 25% methanol. A colony was defined as consisting of 25 to 50 cells or greater. Colonies were counted using a hand-operated clicker.

Integration of survival as a function of dose, or AUC, was calculated form values representing doses 0, 2, 4, and 6 Gy and each allele was compared with its vector control.

Whole Exome Sequencing

Genetic data profiled by The Cancer Genome Atlas (TCGA) were obtained from the Firebrowse (http://firebrowse.org/). Exome capture was performed using paired-end sequencing on the Illumina HiSeq platform. Cancer cell lines were profiled at the genomic level and processed as described in detail (22). The processed data is available for download at http://www.broadinstitute.org/ccle.

RNAseq

RNA was isolated from variant, wild-type, or vector expressing BEAS-2B cells and quantified. mRNA libraries were generated from the total RNA using the Illumina mRNA TruSeq kit following the manufacturer's directions and sequenced using the Illumina HiSeq 5000 platform. The acquired RNA reads were aligned to hg19 genome assembly using STAR (23). RNA counts were normalized within sample and *log* transformed.

Metabolomics

Cells were collected and pellets were flash frozen in liquid nitrogen. Frozen pellets were stored at −80°C until extraction. Samples were thawed and resuspended in 1 mL of ice cold 80% methanol (HPLC grade) and subjected to three freeze–thaw cycles alternating between liquid nitrogen and a 37°C water bath. Next, samples were centrifuged at 20,000 *g* for 15 minutes at 4°C. The resulting supernatants were transferred to fresh tubes and dried. Samples were resuspended in 10 μL per 200,000 cells. Samples were analyzed by high-performance liquid chromatography and high-resolution mass spectrometry and tandem mass spectrometry (HPLC–MS/MS). The sample volumes of 10 μL, which contained 200,000 cells, were injected. Data acquisition and analysis were carried out by Xcalibur 4.0 software and Tracefinder 2.1 software, respectively (both from ThermoFisher, MA).

Information-based association score

The association between the radiation sensitivity profiles (i.e., *log*2 AUC) and single-sample gene set enrichment analysis (ssGSEA) profiles for each gene set or metabolites (∼250 in total) was determined using the information coefficient (IC; ref. 20). ssGSEA enrichment scores were calculated on the basis of the weighted difference of the Empirical Cumulative Distribution Functions of the genes in the set relative to the genes not included in an individual set. The result is a single score per cell line per gene set, transforming the original dataset into a more interpretable higher-level description. Gene sets were obtained from the C2 sub-collection of the Molecular Signatures database, an additional collection of oncogenic signatures, and other cancer-related gene sets curated from the literature, resulting in a dataset that has 4,628 pathway profiles for each sample. ssGSEA values were used as input to compute the *IC*. The nominal *P* values for the information-based association metric scores between the ssGSEA scores, individual metabolites, and radiation response scores were estimated using an empirical permutation test.

Western blot analysis

Whole-cell lysates were prepared using M-PER lysis buffer and clarified by centrifugation. Proteins were separated by SDS-PAGE and transferred onto 0.45 or 0.2 μmol/L nitrocellulose membranes (Maine Manufacturing; Sanford, ME). Membranes were blocked and incubated in primary antibody for 1 to 3 hours at room temperature, washed, and incubated for 1 hour with secondary antibodies. Blots were developed with a chemiluminescence system (Amersham/GE Healthcare).

Microscopy and cellular staining

HCC15 *CTNNB1*Δ cells expressing vector alone or *CTNNB1* variants were plated in a black walled 96-well imaging microplate (Corning, NY) at a density of 1,000 cells/well. Mock and irradiated (6 Gy) cells were fixed and permeabilized 72 hours post treatment using the Image-iT Fixation/Permeabilization Kit (Thermo Fisher Scientific). After fixation, the cytosol and nuclei were stained using actin green probes (green; ThermoFisher, MA) and DAPI (blue; ThermoFisher, MA), respectively. For each cell line, at least 4 wells with 16 images per well (64 images in total) were captured at 40X magnification using a Cytation 5 cell imaging multimode reader (BioTek, VT). All images were processed manually using the ImageJ software. We applied an ellipsoid fit and used size and circularity parameters based on the DAPI intensity to quantify micronuclei (24).

Mouse studies

All animal studies were conducted under protocols approved by the Institutional Animal Care and Use Committees. BEAS-2B cells expressing the designated variants or patient-derived xenografts (PDX) were injected into the flank of NOD.Cg-*Prkdc*^{scid} *Il2rg*^{tm1Wjl}/SzJ (NSG) mice. For PDX studies, biological material was obtained after written informed consent under approval from the Institutional Review Board (IRB). Tumor volumes were measured by caliper and calculated using the formula: (length × width)/2 (2). Mice were randomized into treatment arms when tumors reached ∼200 to 400 mm (3) in volume. Sotorasib (Selleckchem, TX) was formulated according to the manufacturer's specifications and administered at 30 mg/kg to mice daily or every other day based on treatment tolerance. Irradiated mice were anesthetized and protected with a lead shield containing a circular opening overlying the flank. Mice were irradiated using a 320 kVp orthovoltage machine (*XRAD-320* Precision X-ray, CT) at a dose of 0 to 6 Gy (increments of 2 Gy) with a dose rate of 2.17 Gy/min with a source to skin distance of 60 cm using a 1 mm Cu filter. For quality assurance, thermoluminescent dosimeters were used to verify correct dose administration. To establish if intergroup differences were significant, we used regression with random effect and autoregressive errors (25).

Clinical data and statistical analyses

We identified 302 patients treated with high-dose radiation to the lung using stereotactic body radiotherapy from 2010 to 2020. The study, NU00212113, was approved by the Northwestern University IRB and was performed in accordance with the ethical standards as laid down in the 1964 Declaration of Helsinki and its later amendments or comparable ethical standards. Patients with primary (stage I–IV) lung cancer as well as patients with other cancer types comprising solitary or oligometastases to the chest with available next-generation sequencing (NGS) data were included. Mutation status was determined using pyrosequencing technology for 2 genes (*KRAS* and *EGFR*) or NGS panels of 22 or 161 genes based on routine clinical care at Northwestern University (Chicago, IL) from 2010–2020. A total of 85 and 107 patients were profiled for *KRAS* and *CTNNB1* mutational status, respectively. Radiation treatment failure was defined as radiographic progression within 1 cm of the planning target volume to maintain a consistent definition of local/marginal failure in clinical trials of stereotactic body radiation therapy (26). CT scan(s), followed by at least one PET/CT, determined radiographic progression. A maximum

SUV exceeding the initial pretreatment PET scan or serial increases in SUV on posttreatment PET scan was considered a local failure. If PET/CT findings were consistent with failure, a biopsy was requested. Prescription radiation dose was adjusted for the number of fractions of radiation by calculating the biologically effective dose (BED) with a standard α/β ratio of 10. Length of follow up was determined from the end date of radiotherapy and patients who had not died were censored at the time of last chest imaging. Cumulative incidence curves for local failure were estimated using the competing risk method, and Gray test was used to determine significance between cumulative incidence curves (**27**). Statistical analysis was performed using R 4.1.2 (The R Foundation, Vienna, Austria; ref. 28).

Data availability

The RNA sequencing data has been deposited in the Gene Expression Omnibus database (GSE216711). Genomic data pertaining to cancer cell lines was downloaded from the CCLE (http://www.broadinstitute.org/ccle). Other datasets analyzed during the current study are available within the article, its supplementary files, or from the corresponding author upon request.

Code availability

All custom or modified code is available upon request. There are no restrictions to access.

Results

Inter- and intra-gene variation in survival after irradiation

We nominated single-nucleotide variants (SNV) that have a higher likelihood of altering the sensitivity of cells to radiation using a new *in silico* pipeline (**Fig. 1A**). We first measured the mutual dependence or IC between the radiation sensitivity profiles of 533 cancer cell lines and SNV features (20, 22). The IC metric has several advantages compared with monotonic methods of regression, including higher sensitivity to nonlinear associations and significantly better resolution at the extreme ends of the radiation sensitivity matching ranges (29). We nominated variants using two complementary labeling methods: (i) variants in the gene of interest, yes [1] versus no [0] or (ii) variants in a structured domain by UniProt (30) of the gene of interest, yes [1] versus no [0]. The latter design was used to improve the detection of functional variants because structural domains frequently contain residues that are critical for maintaining domain stability and, hence, gene function. Variants derived from commonly mutated genes (CMG) (>2% frequency) as annotated by TCGA in pan-cancer studies (31) and 22 variants with no mutual association (NMA; IC $\sim$ 0) with radiation sensitivity were also included to assess the performance of *in silico* enrichment. Altogether, 488 alleles (396 SNVs) from 92 genes were generated and profiled.

Because it can be difficult to contextualize the role for a particular variant within distinct genetic backgrounds (11), we implemented a systematic, arrayed approach using a cell with minimal background genetic alterations. Whole-exome sequencing (WES) of the adenovirus-12 SV40 hybrid transformed immortalized upper airway bronchial epithelial cells, or BEAS-2B (32), showed no known oncogenic or tumor suppressor mutations (Supplementary Data 1). Moreover, BEAS-2B cells were amenable to high-content radiation survival profiling, were clonogenic, and were previously shown to undergo oncogene-driven transformation, thus facilitating both testing and downstream validation (12).

Putative gain-of-function (GOF) variants were stably integrated and tested in an arrayed format using a previously benchmarked high-content radiation platform (**Fig. 1B**; refs. 10, 20). To characterize LOF variants, ORFs were stably integrated into a genetically modified BEAS-2B lacking the respective gene (i.e., *KEAP1* and *TP53BP1*, see below). After irradiation, we measured integrated survival as a function of dose, normalized to in plate vector control, and *log*2 transformed the ratio (Supplementary Data 2). The signal-to-noise ratio between $NFE2L2^{E79K}$ and vector alone was 1.19 ± 0.09 and was stable for the duration of the profiling period (Supplementary Fig. S1). To benchmark the platform with other measures of radiation survival, high-content survival values for a subset ($n = 39$) of the alleles profiled were compared with values from the clonogenic assay (for each cell line, $n \geq 2$; Supplementary Fig. S2). High-throughput and colony integral outputs were significantly correlated (Pearson $r = 0.43$ and $P = 0.007$).

A scatter plot of radiation survival values demonstrated variants in genes that impacted signal transduction, cell cycle, gene transcription (via transcription factors), and cellular metabolism (**Fig. 1C**; Supplementary Fig. S3). Critically, there was significant variation in survival across and within individual genes. To assess differences in the distribution of response across some profiled genes, we plotted the probability density distribution of survival values (**Fig. 1C**, inset). Some genes had unimodal changes in radiation sensitivity (i.e., *TGFBR1*) whereas other had bi- or multimodal distributions. Interestingly, *CTNNB1* had a bimodal distribution that spanned a wide range of sensitivity, potentially reflecting diametrically distinct functional variants within the same gene. A confluence of impactful variants clustered at hotspots residues in some genes, whereas other genes did not demonstrate residue or structural domain selectivity (Supplementary Fig. S4). Importantly, *in silico* nominated variants had wider ranges of radiation sensitivity compared with variants from CMGs or with NMA based on cancer cell line profiling (Supplementary Fig. S5). Taken together, systematic radiation sensitivity profiling of unary variants in BEAS-2B cells revealed significant inter- and intra-gene variation and our *in silico* nomination pipeline significantly improved salient variant detection.

Characterization of gene variants associated with radiation survival

The distribution of radiation sensitivity indicated that genetic variants altered the radio-phenotype along a continuum (**Fig. 2A**). We measured the dynamic range of the platform using benchmarked genetic alterations for radiation resistance and sensitivity: $NFE2L2^{E79K}$ and *TP53BP1*Δ, respectively. $NFE2L2^{E79K}$ has been shown to confer resistance to radiation (10, 20) and *TP53BP1* functions in DNA repair and its deletion has been shown to confer radiation sensitivity (33). Using the SD (σ) as cut points, we classified variants into resistant, sensitive, or functionally neutral groups. Using these criteria, 22%, 10%, and 68% of the variants were resistant, sensitive, or neutral, respectively.

Because radiation sensitivity in cancer cell lines informed the selection of our nominated variants (see **Fig. 1A**), we measured the association between variants and corresponding cancer cell line sensitivity (**Fig. 2B**). We found a significant association between the two platforms, suggesting that previous biological outputs of radiation sensitivity (10) coupled with structured protein domain-based enrichment can significantly improve functional variant identification. Because the measured association spanned distinct cancer types and cell lines, these results also suggested that some variants can alter radiation sensitivity across distinct genetic backgrounds.

We compared functional variants in our platform with classifications from other variant interpretation tools (**Fig. 2C**; Supplementary

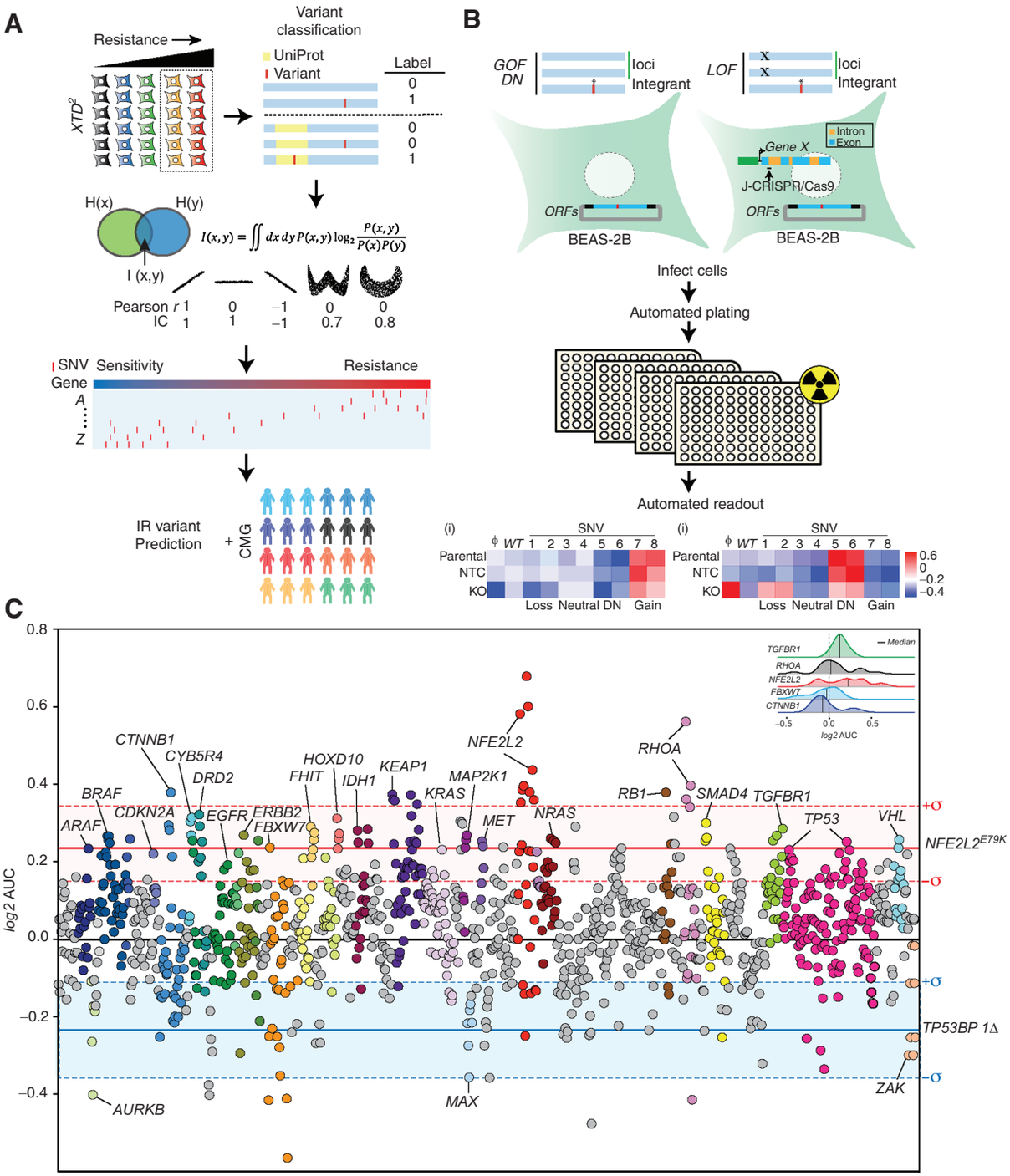

Figure 1.

High-content profiling of common and rare genetic variants for radiation sensitivity. **A,** Computational pipeline for the nomination of candidate SNVs. Associations were measured using the IC. The variant candidate list was supplemented with CMGs in cancer if they were not directly nominated by the pipeline and 22 variants with IC ∼ 0. **B,** Wild-type or variant-expressing ORFs of genes were stably integrated into BEAS-2B cells and tested in an arrayed format (unique SNV per well) using a high-content radiation platform. Heatmaps depict interpretation schemas for categories of variants under conditions in which loss of gene function results in radiation (i) sensitivity or (ii) resistance. **C,** Radiation sensitivity was measured for all profiled variants [488 unique alleles; 1,180 biological replicates (at least 2 replicates per variant)] by AUC calculations across 4 conditions (ϕ, 2, 4, or 6 Gy), followed by normalization using vector control in the sham irradiated (ϕ) plate per tranche, and then *log2* transformed. Each variant was measured in biological replicates (two distinct vector clones). A number of 92 tested genes are arranged alphabetically and some of genes are labeled with color match for ease of visualization. The mean ± SD (σ) for established resistant and sensitive alleles *NFE2L2*^{E79K} and *TP53BP1*Δ, respectively, are shown to delimit the dynamic range of radiation sensitivity in the platform.

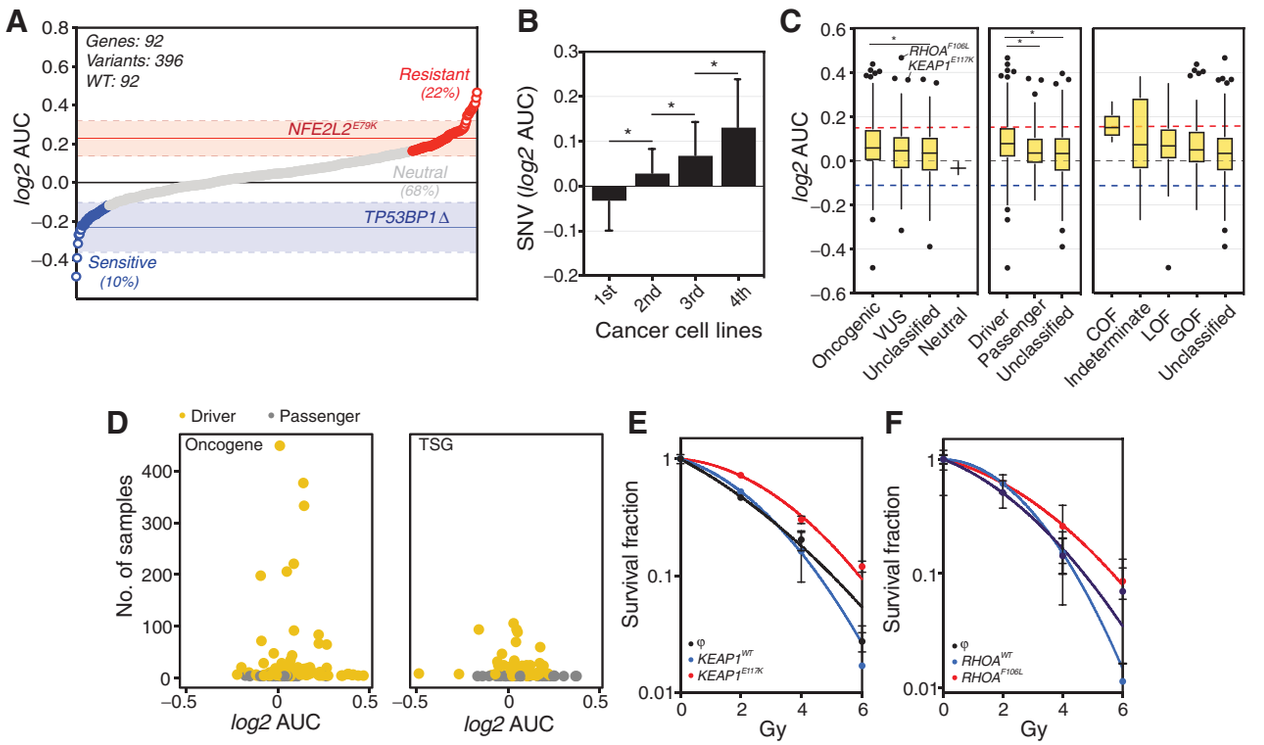

Figure 2.

Characteristics of SNVs that alter the radio-phenotype. **A,** 488 (396 SNVs and 92 associated wild-type) alleles are displayed. Each value represents one biological replicate. Radiation sensitivity was discretized into categories of resistant and sensitive based on > *NFE2L2*^{E79K} median −σ (red) and < *TP53BP1*Δ median +σ (blue), respectively. **B,** Variants represented in cancer cell lines previously profiled for radiation survival were partitioned into quantiles (1st, the most sensitive; 4th, most resistant). SNVs profiled in (**A**) were binned on the basis of the presence of the SNV in a cell line within the designated quantile. The *log*2 AUC from (**A**) were then plotted by column plot, stratified by quantiles. Column height represents the mean and error bars represent SD. *, *P* values < 0.0001 by Welch *t* test. **C,** Boxplots represent classification of profiled variants into categories defined by databases OncoKB (oncogenic and functional status) and MutaGene (driver or passenger). Variants that were not found in either database were labeled "unclassified". **D,** Scatter plots of variants identified as oncogenes or tumor suppressor genes (TSG) in samples sequenced by WES. **E,** BEAS-2B cells stably infected with vector alone (ϕ) or *KEAP1*^{WT} or *KEAP1*^{E117K} were irradiated and the survival fractions were measured at day 9–10 by the clonogenic assay. Data points represent mean ± SEM. Bar plots represent the indicated *NFE2L2* expression signatures measured in BEAS-2B cells. **F,** BEAS-2B cells stably infected with vector alone (ϕ), *RHOA*^{WT}, or *RHOA*^{F106L} were treated with ionizing radiation and the survival fractions at day 9–10 were measured by the clonogenic assay.

Data 3; refs. 34, 35). We found that overall, oncogenic variants were the most likely to confer radiation resistance, followed by variants predicted to be of unknown significance (VUS), unclassified, and neutral. Similarly, predicted driver variants were most likely to confer resistance, followed by passenger and unclassified variants. Functional impact type, however, was not associated with radiation sensitivity suggesting that both GOF and LOF variants can similarly impact radiation sensitivity. To determine the association between radiation sensitivity and the frequency of variants in cancer, we compared the two variables stratified by gene type: oncogene versus tumor suppressor (**Fig. 2D**; ref. 36). Most variants that altered radiation sensitivity had a low rate of occurrence in cancer, irrespective of their gene classification.

Despite the overall trends, there were many oncogenic and driver variants that did not alter radiation sensitivity. Moreover, several variants conferred a strong phenotype despite the lack of previously established clinical or biological significance. For example, *KEAP1*^{E117K} and *RHOA*^{F106L} conferred radiation resistance despite their classification as VUS (**Fig. 2C**, **E** and **F**). For *KEAP1*^{E117K}, gene expression gene set analysis demonstrated activation of the Nrf2 pathway indicating a dominant negative effect (Supplementary Fig. S6). These results indicated that phenotypic profiling represents a more sensitive methodology for annotating impactful variants.

Genetic addback reveals distinct categories of variants

LOF variants associated with genes that impact radiation sensitivity are unlikely to be identified unless they also confer dominant-negative effects in parental BEAS-2B cells. We devised a *j*-CRISPR strategy to ameliorate this profiling gap. Junctional refers to design of a sgRNA that spans the exon-intron junction of the target gene loci. After knockout, variant-expressing ORFs are predicted to be resistant to the introduced guides because they lack introns. Although genetic addback could be achieved using other approaches (37, 38), *j*-CRISPR offers the facile and highly efficient means to effect the biallelic loss of target genes (39) while retaining the capability to use our large-scale SNV library in its current form.

We benchmarked *j*-CRISPR using the tumor suppressor genes, *KEAP1* and *TP53BP1* (**Fig. 3**). sgRNAs that target the exon 2::intron 2–3 junction of *KEAP1* and the exon 5::intron 5–6 junction of *TP53BP1* were used to delete each target gene. After infection, selection, and monoclonal outgrowth, Sanger sequencing from a representative *KEAP1* knockout (*KEAP1*Δ) clone identified a homozygous

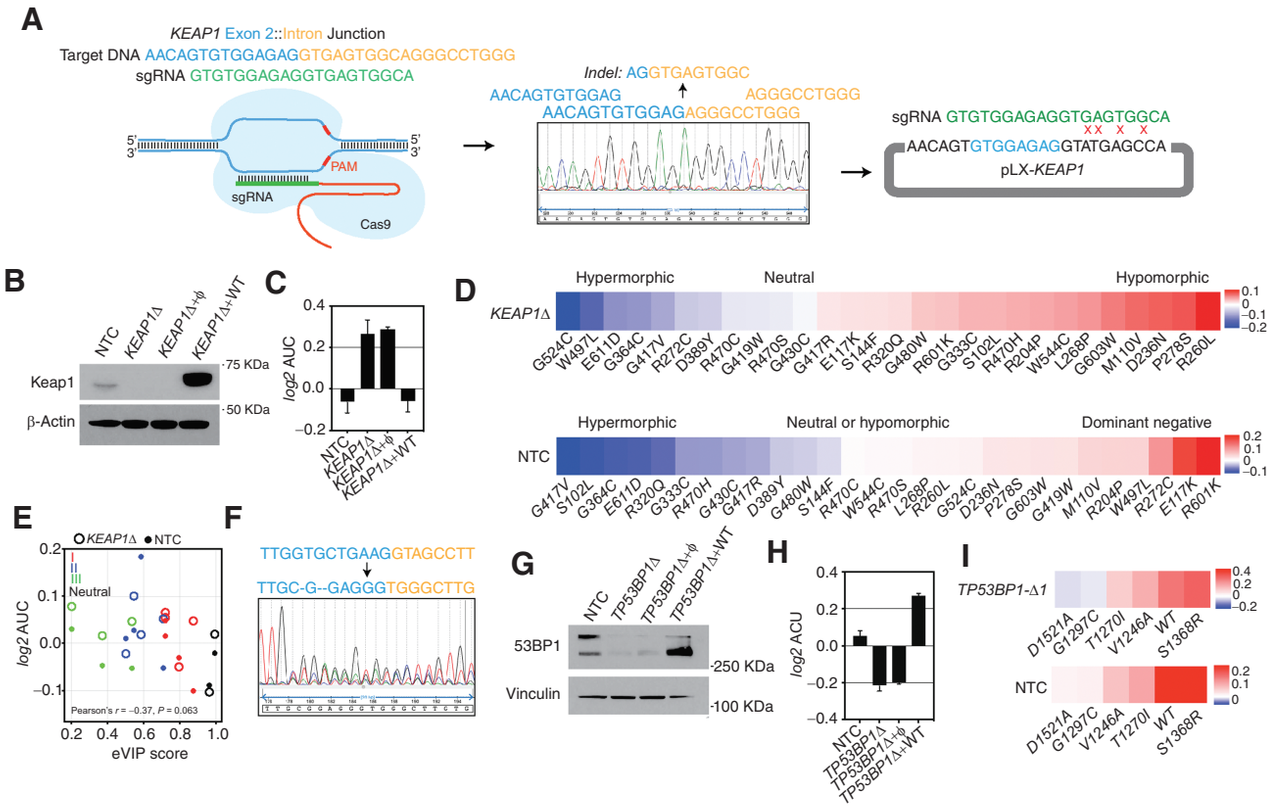

Figure 3.

j-CRISPR/Cas9 knockout of *KEAP1* or *TP53BP1* followed by genetic addback identifies categories of SNVs that impact radiation sensitivity. **A,** Schematic depiction of the *KEAP1* sequence at the exon 2-intron junction. A representative sgRNA is shown in green. A representative sequence (chromatogram) of the exon2-intron junction is shown. Gene inactivating sgRNA result in internal deletions (indels) of varied length at the junction (representative indel is shown). The sgRNA is predicted to not bind the spliced ORF due to sequence heterology (mismatch). **B,** Immunoblots and (**C**) radiation survival analysis of a representative BEAS-2B *KEAP1*Δ clone alone or with vector control (ϕ) or wild-type *KEAP1*. Cells expressing NTC guides were characterized for baseline protein expression and radiation survival. **D,** Radiation survival of either (top) *KEAP1*Δ or (bottom) NTC cells expressing the indicated *KEAP1* variants (29 in total). Each heatmap was normalized to an expression vector control cell line and then to wild-type *KEAP1* and ordered on the basis of *log2* AUC [most sensitive (blue) to most resistant (red)]. Labels (hypermorphic, neutral, hypomorphic, or dominant negative) indicate putative categories of mutations in *KEAP1*. **E,** Scatter plot of the radiation survival of a subset of *KEAP1* variants categorized as class I, II, III, or neutral mutations based on eVIP scores (15). **F,** Representative sequence (chromatogram) of the exon5-intron junction of *TP53BP1*Δ pooled clones. **G,** Immunoblots and (**H**) radiation survival analysis of a representative BEAS-2B *TP53BP1*Δ pooled clones expressing the indicated guides alone or with vector control (ϕ) or with expression of wild-type *TP53BP1*. Cells expressing NTC guides were also characterized for baseline protein expression and radiation survival. **I,** Radiation survival of either (top) *TP53BP1-Δ1* or (bottom) NTC cells expressing the indicated *TP53BP1* variants (5 in total). Each heatmap was normalized to an expression vector control cell line (i.e., NTC cells expressing destination vector alone).

indel mutation in proximity to the predicted cleavage site (**Fig. 3A**). To examine whether the cleavage point is resistant to the introduced synthetic guide, we introduced the *KEAP1* ORF and demonstrated the stable expression of *KEAP1* (**Fig. 3B**). Critically, the addback of *KEAP1*, despite its higher levels of protein expression, reversed the *KEAP1*Δ resistance phenotype to baseline sensitivity levels (**Fig. 3C**). We introduced 29 *KEAP1* variants into both single-guide non-targeting control (sgNTC) and *KEAP1*Δ cells and measured radiation survival (**Fig. 3D**). It was evident that *KEAP1* variants had a wide range of impact on the sensitivity of cells to radiation across the sensitivity spectrum. In addition, *KEAP1*Δ cells demonstrated an increased ability to resolve LOF variants compared with sgNTC cells.

We normalized survival values to *KEAP1* wild-type levels and classified variants based on phenotypes across cellular contexts into neutral, dominant-negative, hypomorphes, or hypermorphes. Intriguingly, we identified *KEAP1* variants that had increased levels of activity compared with wild-type *KEAP1*, resulting in greater radiation sensitivity. A class of *KEAP1* variants have been previously shown to have an enhanced ability to bind Nrf2 (i.e., super-binders), resulting in the modulation of Nrf2 activity (40). Our data adds to this list of putative super-binders (e.g., R272C; ref. 41) and reveals the complexity inherent in biomarker classification for putative radiation resistance biomarkers like *KEAP1*. We also compared *KEAP1* variant sensitivity to a gene expression-based phenotypic impact profiling method, eVIP (15). eVIP scores derived from variant expression in the *KEAP1* G333C mutant cancer cell line, A549, showed some overall concordance across categories of variants (**Fig. 3E**). Despite this trend, there was a wide range of sensitivity values within eVIP classes and scores, indicating a greater capability for our experimental assay in discerning phenotypic impact.

Using an analogous approach, we targeted a critical element of DNA repair and cell-cycle regulation, *TP53BP1* (33, 42). Sanger sequencing from a polyclonal mixture of *j*-CRISPR edited *TP53BP1*Δ cells showed multiple sequences around the expected cleavage point (**Fig. 3F**).

*TP53BP1*Δ cells demonstrated significant radiation sensitivity compared with sgNTC cells (**Fig. 3G**). We introduced the *TP53BP1* ORF expressing either wild-type or 5 gene variants associated with radiation hyper-sensitivity based on cancer cell line data. Wild-type *TP53BP1* addback to *TP53BP1*Δ cells reversed the sensitivity phenotype to levels greater than baseline (sgNTC), indicating that *TP53BP1* overexpression can enhance response to radiation-induced cell death (**Fig. 3H**). Four of 5 (80%) of the tested variants showed a range of hypomorphic activity compared with wild-type. Functional variant D1521A mapped to the Tudor domain, V1246A and T1270I mapped to the oligomerization domain, and G1297C is within an unstructured region between the Tudor and oligomerization domains. These results indicated that like *KEAP1*, *TP53BP1* variants span a range of gene activity and provide additional evidence that cancer cell line radiation sensitivity profiling can improve functional variant identification.

Cellular context, *in vivo*, and inter-genic effects on variant impact

The frequencies of variants across cancer types can vary on the basis of the tissue of origin, tumor microenvironment, and the underlying mutagen or mutational process (43). Moreover, organ and environmental context can impact oncogenic signaling and phenotypes (44). To determine the context-specificity of impactful variants, we sought to assess the cellular, environmental, and inter-genic effects on the radio-phenotype. First, we identified 18 variants that conferred resistance to radiation in the BEAS-2B cell line. We introduced these variants and their wild-type alleles ($n = 9$) into the lung squamous carcinoma cell line NCI-H520 and the hTERT immortalized urothelial cell line TRT-HU1 (**Fig. 4A**). Despite some variability in the magnitude of resistance for some variants, the resistance phenotypes were largely concordant across cellular contexts; most alleles that were resistant in the BEAS-2B cells were also resistant in NCI-H520 and TRT-HU1 cells (by Clopper–Pearson intervals; **Fig. 4B**), indicating that impactful variants were mainly cellular context indifferent.

We next sought to assess the impact of tumor microenvironment on radiation sensitivity using a murine xenograft tumor model. We injected several BEAS-2B lines expressing *NRAS*, *KRAS* or *EGFR* variants that conferred variable levels of radiation resistance *in vitro* into the flank of NSG mice (**Fig. 4C**). Consistent with their oncogenic roles, all injected variants led to tumor engraftment and growth. Mice bearing BEAS-2B cells expressing the indicated variants were block randomized into sham (ϕ) or irradiated cohorts (2, 4, and 6 Gy; single fraction) and monitored for tumor growth delay (Supplementary Fig. S7). The intra-gene rank order of resistance was concordant for all 3 genes. For example, *NRAS* Q61K, G13R, and G12C were the most to least resistant variants to radiation both *in vitro* and *in vivo*. Moreover, the rate of tumor growth as measured by time to 1 cm^3 and *in vitro* derived survival fraction measurements were correlated across all doses (2, 4, and 6 Gy) (Spearman's $r = -0.53$; $R^2 = 0.28$; $P < 0.01$), with variants that conferred greater resistance demonstrating a shorter time to 1 cm (**Fig. 4D**; ref. 3). These results indicated some concordance between *in vivo* and *in vitro* sensitivity measures.

We also examined the influences of genetic context on individual impactful variants. First, we used genetic data profiled by TCGA ($n = 10{,}967$ tumors) to identify co-occurring alterations with genes implicated in radiation resistance. We generated whole-exome covariate association P and q values across the top 10 genes associated with radiation resistance and found a strong association between alterations in *STK11* and radiation-resistant genes *KEAP1* and *KRAS* [*log2* odds ratio of 3.8 and 1.39, respectively; ($P < 0.001$, $q < 0.001$)]. *STK11* is frequently inactivated in lung adenocarcinoma and leads to both increased primary tumor growth and the acquisition of metastatic potential (45, 46). Consistent with these observations, Upset and Venn plots showed the respective genes to be significantly co-altered in lung adenocarcinoma (**Fig. 4E** and **F**).

We examined the interactive effects of the respective co-altered genes on radiation sensitivity. We deleted *STK11* and *KEAP1* alone and together in BEAS-2B cells (**Fig. 4G**). *KEAP1*Δ, but not *STK11*Δ, resulted in radiation resistance. However, *KEAP1*Δ/*STK11*Δ co-deleted cells showed a significant increase in radiation resistance compared with *KEAP1*Δ alone (**Fig. 4H**). We also integrated into NTC or *STK11*Δ cells several *KRAS* variants and measured the impact of the deletion on radiation sensitivity. The integral survival of the *KRAS* variants were generally higher in *STK11*Δ cells, although this effect varied across individual variants (**Fig. 4I** and **J**). Together, these results indicated that genetic co-alterations cooperate to amplify the resistance of *KEAP1* and *KRAS* altered cells.

Integrative multiomic profiling of impactful variants

We used ssGSEA projections to identify gene expression pathways that are associated with radiation sensitivity. We compared the profiles of 4,628 gene set/pathway with the radiation sensitivity values across 42 alleles (**Fig. 5A**). The top gene sets associated with radiation resistance represented pathways including transmembrane transport, cellular signaling (e.g., Ras, MAPK, TGFβ, RhoA), and lipid metabolism, among others (Supplementary Data 4). Gene sets associated with transmembrane transport activity included, in part, genes associated with amino acid transport like xCT (*SLC7A11*) and ASCT2 (or *SLC1A5*). xCT is the light chain subunit of cystine/glutamate antiporter system xc- and ASCT2 is the neutral amino transporter that preferentially transports glutamine (47). By regulating the levels of essential glutathione precursors, namely cysteine and glutamine, these transporters play a vital role in maintaining redox homeostasis. Consistent with these roles, a directed analysis of genes associated with glutathione synthesis including *GLS2*, *GCLM*, *GCLC*, and *GSR* demonstrated significant associations with radiation resistance (**Fig. 5B** and **C**; Supplementary Data 5). These results suggest that the plurality of variants associated with radiation resistance rewire the transcriptome to improve oxidative reductive capacity, putatively by increasing glutathione levels.

To validate these findings, we profiled > 250 metabolite targets comprising sentinel analytes in BEAS-2B cells expressing selected impactful variants. Global pathway enrichment analysis revealed, in part, nucleotide, glutamate, and glutathione metabolism as highly associated with radiation resistance (Supplementary Fig. S8). These pathways have been previously shown to be linked, mainly by glutamine metabolism (48). In addition to glutamine representing a critical precursor for glutathione synthesis, the synthesis of the pyrimidine nucleotides begins with the formation of carbamoyl phosphate from glutamine and CO_2. In purine nucleotide synthesis, nitrogen at N3 and N9 are contributed by the amide group of glutamine. Consistent with these observations, metabolomic analysis revealed that the end products of nucleotide synthesis were elevated in radioresistant cells, accompanied by increased levels of some important intermediates (**Fig. 5C**; Supplementary Fig. S9).

We associated levels of individual metabolites with radiation survival using the IC association metric (**Fig. 5D**; Supplementary Data 6). Consistent with gene and gene set expression correlations of increased amino acid cellular uptake and glutathione synthesis, there was a significant association between the levels of glutathione, glutamine-

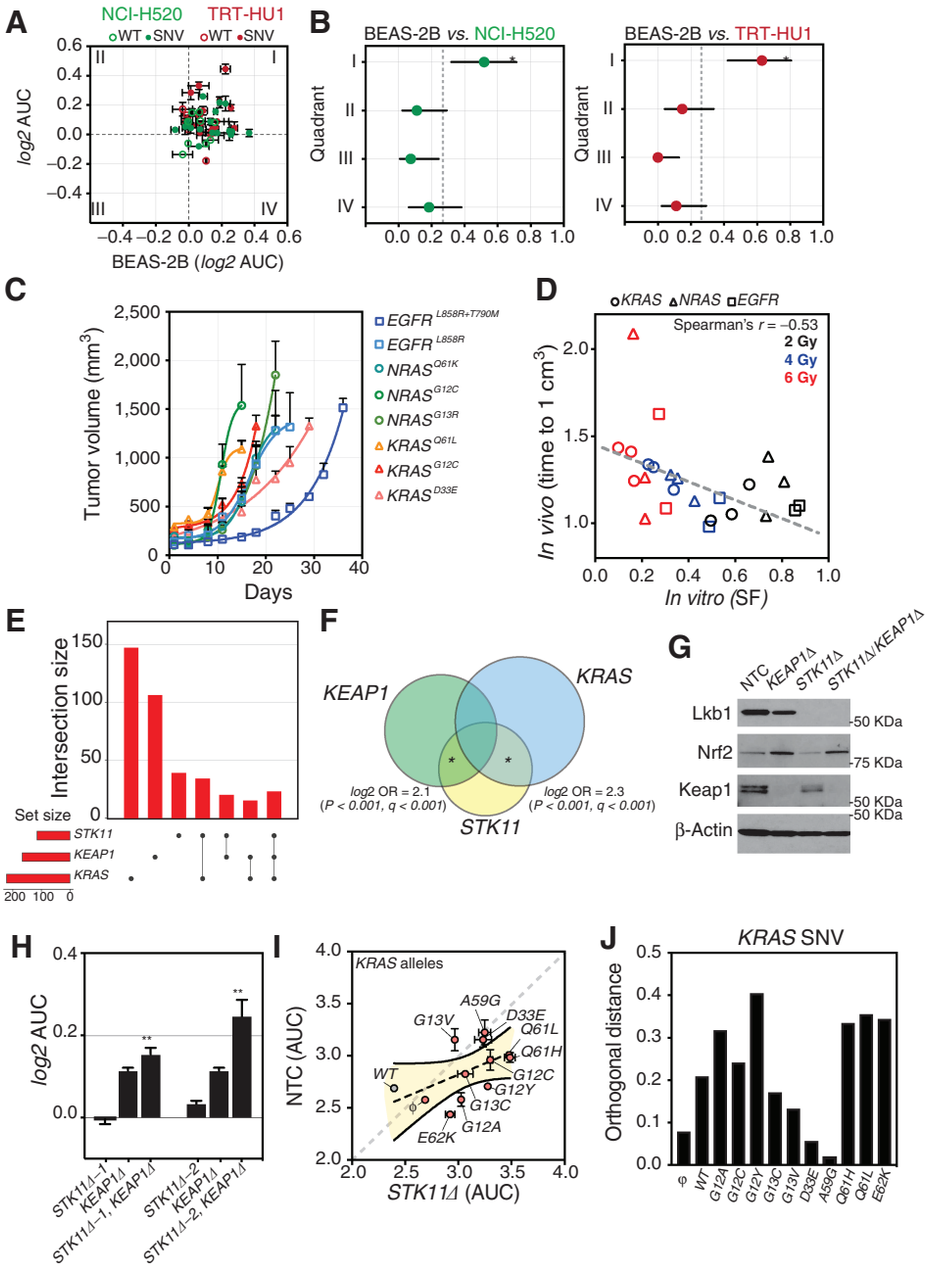

Figure 4.

The impact of cellular context, tumor microenvironment, and co-occurring genetic events on SNVs associated with radiation resistance. **A,** Scatterplot of radiation survival values for 27 alleles (9 wild-type and 18 variants) expressed in the indicated cell lines. Data are expressed as the means ± SEM. **B,** The proportion of alleles (variants and wild-type) that localized to each cartesian quadrant (I–IV) are shown. 95% CIs were calculated by the binomial proportion CI (Clopper–Pearson). An * indicates CIs that do not cross the (random dart) estimate of 25% of variants per quadrant. **C,** BEAS-2B cells expressing the indicated variants were injected into the flank of NSG mice and measured for tumor growth. **D,** Mice were block randomized into the following treatment arms: sham (ϕ) or X-ray (2, 4, or 6 Gy). Scatter plot and linear regression of *in vitro* radiation survival values (SF, surviving fraction) and *in vivo* tumor growth delay after irradiation (normalized to ϕ). **E** and **F,** Upset and Venn diagram plots for co-occurrence of *KRAS, KEAP1*, and *STK11* alterations comprising gene mutations or deep deletions of *KEAP1* or *STK11* in lung adenocarcinoma tumors from TCGA. The *log2* odd ratios, *P*, and *q* values for co-occurrences are shown. *, *P* and *q* values < 0.05. The top 10 'resistant genes' were identified using a rank order (highest to lowest) of SNV survival fraction at 6 Gy. They included: *NFE2L2, EGFR, KEAP1, U2AF1, IDH2, STK11, TP53, FBXW7, RBM45*, and *KRAS*. **G,** Immunoblot and (**H**) radiation survival of NTC, *KEAP1*Δ, *STK11*Δ, or *KEAP1*Δ/*STK11*Δ in BEAS-2B cells. **, *P* value < 0.05 for interaction based on two-way ANOVA test. Two distinct sgRNA targeting *STK11* were tested (Δ-1 and Δ-2) for radiation survival. **I,** Wild-type or variant-expressing *KRAS* were introduced into either NTC or *STK11*Δ cells. Radiation survival, measured by AUC, for the indicated alleles or vector control (ϕ). Scatter plot and linear regression with 95% confidence band of the best-fit line are shown. **J,** Orthogonal distance measurements to the line of equality (diagonal) for each allele in (**I**).

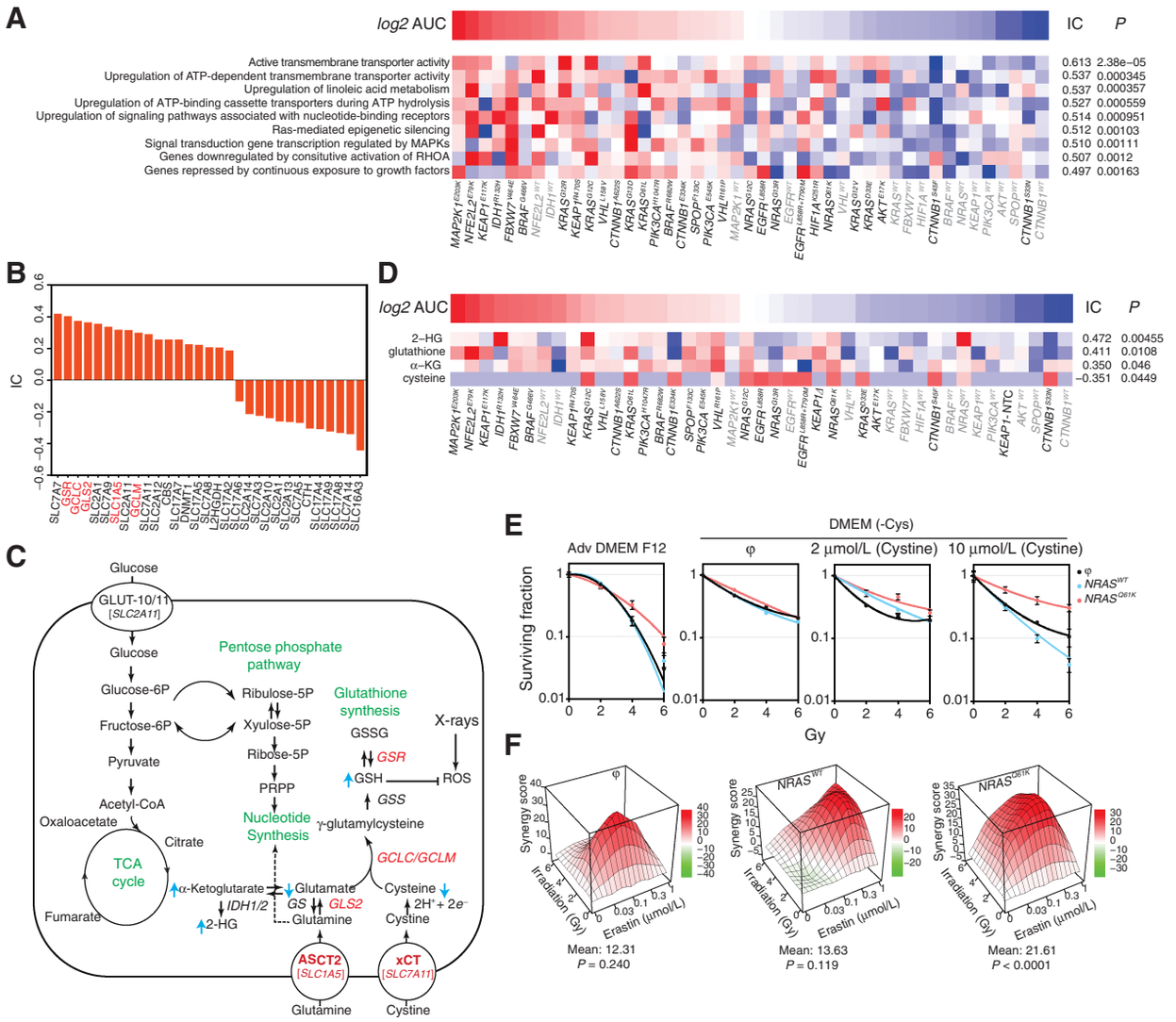

Figure 5.

SNVs can reconfigure the transcriptome and metabolome to enhance survival after irradiation. **A,** single sample, (**B**) single-gene GSEA, and (**D**) ssMETA analyses identify gene sets, genes, and metabolites respectively, that correlate with resistance to radiation across 42 profiled alleles (12 wild-type, 30 variants). Heatmap of enrichment scores (red, positive; blue, negative). A subset of the top gene sets, genes, and metabolites are shown. **C,** Schematic of the metabolic pathways associated with radiation resistance. Genes depicted in red font [similarly demarcated in (**B**)] are associated with amino acid (i.e., cystine and glutamine) transport and glutathione synthesis. Blue arrows indicate the direction of metabolite level changes associated with resistance. **E,** Variant-expressing BEAS-2B cells were grown in cysteine dropout media supplemented with vehicle or cystine at the indicated concentrations and treated with ionizing radiation. The survival fraction at 7 to 8 days after irradiation is shown. Data are expressed as the means ± SEM. **F,** Cells were treated with erastin for 24 hours followed by mock treatment or irradiation at the indicated doses. The survival fraction at 7 to 8 days after irradiation is shown. The mean synergy score from a HSA model are shown. The significance of the difference between the estimated mean synergy score compared with the null hypothesis of non-interaction are shown (*P* value).

derived metabolites (α-ketoglutarate and 2-HG), and cysteine with radiation resistance. These data suggested that variants that conferred resistance to radiation increased glutathione synthesis, in part by facilitating amino acid uptake and metabolism. We noted that cysteine levels were notably higher in *EGFR* and *RAS* variant-expressing cells. We, therefore, posited that cystine deprivation would have a greater impact on the sensitivity of these variants compared with their wild-type counterparts. Indeed, cystine dropout had marginal effects on wild-type allele-expressing or vector control cells but significantly diminished the magnitude of radiation resistance in $NRAS^{Q61K}$-expressing cells (**Fig. 5E**). Importantly, cystine addback restored radiation resistance in cells expressing Q61K but not wild-type *NRAS* or vector alone cells. Altogether, these results indicated that rewiring the metabolome to increase uptake of essential glutathione precursors represents a critical mechanism for conferring radiation resistance for some variants.

On the basis of the role of xCT in therapeutic resistance in some variants, we predicted that the xCT inhibitor, erastin, can function as a sensitizer in cells expressing select variants (49). Indeed, $NRAS^{Q61K}$-expressing cells treated with erastin and radiation showed a synergistic

decrement in clonogenic survival [highest single agent (HSA) mean = 21.61; $P < 0.0001$; null hypothesis indicating non-interaction; **Fig. 5F**]. Vector alone and wild-type *NRAS*-expressing cells showed less synergy with radiation. These results indicate that xCT inhibitors can be potent therapeutic sensitizers in cells containing categories of radiation-resistant variants, nominating combinatorial treatments as a potentially effective treatment strategy in tumors that are driven by these variants.

Categories of *CTNNB1* mutations differentially alter radiation sensitivity

The top gene sets associated with radiation sensitivity represented pathways including cell cycle (i.e., G_2–M progression), RNA processing, and nuclear structure, among others (Supplementary Data 4). β-catenin activity, driven by exon 3 variants in *CTNNB1*, were highly correlated with radiation sensitivity and active for gene sets associated with progression through anaphase via the anaphase promoting complex (APC; **Fig. 6A**). Exon 3 of *CTNNB1* encodes several serine-threonine phosphorylation sites that regulate the stability and nuclear localization of β-catenin (50). Mutations in exon 3 have been associated with the nuclear accumulation of β-catenin resulting in constitutive Wnt/β-catenin signaling. In contrast to the exon 3 containing N-Terminal (NT) domain, the armadillo repeats (ARM) and the C-Terminal (CT) domain of *CTNNB1* are less commonly mutated (**Fig. 6B**; ref. 31). The functional impact of these variants, if any, remains unclear.

We noted a trend toward differential sensitivity in cancer cell lines with mutations in the NT versus the ARM domains (**Fig. 6C**). To examine these effects directly, we introduced the *CTNNB1* ORF expressing either wild-type or 16 variants spanning all domains into BEAS-2B cells and measured radiation sensitivity. Consistent with cell line data trends, we showed that exon 3 variants conferred radiation sensitivity (**Fig. 6D**). Moreover, mutations in the ARM domain were significantly more likely to confer radiation resistance [*log*2 AUC 95% confidence interval (CI), 0.28–0.24; $P = 0.02$; one sample *t* test]. These results indicated that mutations in *CTNNB1* can have diametrically opposed effects.

To study the impact of *CTNNB1* variants in a cancer context, we performed *j*-CRISPR deletion of *CTNNB1* in HCC15, a lung squamous cell carcinoma cell line with an activating missense mutation in exon 3, S45F (**Fig. 6E**). *CTNNB1*Δ cells were significantly more resistant to radiation compared with NTC cells (**Fig. 6F**). The addback of the same 16 *CTNNB1* variants to the HCC15 *CTNNB1*Δ cells demonstrated a radiation sensitivity profile like that observed in BEAS-2B cells (**Fig. 6G**). NT mutant-expressing cells had higher levels of β-catenin localized to the nucleus, consistent with their hypermorphic activity (**Fig. 6H**). In contrast, some ARM domain mutant-expressing cells had substantially lower cellular β-catenin levels, indicating a potential dominant negative role for a subset of these mutants.

We examined the impact of unchecked progression through anaphase via the APC in categories of *CTNNB1* variants. We posited that cell-cycle progression despite DNA damage could result in higher rates of mitotic catastrophe in cells expressing exon 3 mutants. To test this, we quantified chromosomal instability after irradiation by measuring the number of micronuclei (**Fig. 6I** and **J**). HCC15 expressing exon 3 variants had substantially higher micronuclei than vector alone cells. Conversely, ARM domain mutant (V600G)-expressing cells had lower numbers of micronuclei. These results suggest that hypermorphic *CTNNB1* mutants confer radiation sensitivity by increasing the probability of mitotic catastrophe after irradiation.

To examine the clinical relevance of the *CTNNB1* variants, we identified patients with primary lung cancer or other cancer types that metastasized to the chest who were treated with high-dose radiotherapy alone to these index lesions. We annotated cases for local failure outcomes, which we defined as radiographic progression within the irradiated volume (**Fig. 6K**). Patients with *CTNNB1* mutant tumors were younger, more likely to have non–lung primary metastases, more likely to be treated with oligometastatic intent, and had longer median follow-up and overall survival (Supplementary Table S1). The two groups had otherwise similar patient, tumor, and treatment characteristics. 107 patients from our cohort underwent *CTNNB1* exon 3 genotyping; 11 patients had tumors with *CTNNB1* mutations. Patients with *CTNNB1* mutant tumors had a significantly lower rate of local treatment failure than those with *CTNNB1* wild-type tumors, with 3-year cumulative incidences of 27.9% (95% CI, 16.0%–38.1%) and 0% (95% CI, not applicable), respectively (**Fig. 6L**). Importantly, there were no significant differences in the radiation dose delivered (Welch *t* test, $P = 0.12$) or tumor size (Welch *t* test, $P = 0.21$; **Fig. 6M**) between patients with mutant or wild-type *CTNNB1*. A multivariate regression model that included *CTNNB1* gene status, tumor size, and dose showed that *CTNNB1* mutation status as the only variate that remained significant (Supplementary Table S2).

KRAS variants confer resistance to high-dose radiation

Most variants increased survival consistently across the tested dose range (2–6 Gy; Supplementary Data 2). However, there were exceptions to this trend. In particular, *KRAS* variants showed enhanced survival selectively at the highest doses of radiation (**Fig. 7A**). To confirm these findings, some *KRAS* variants were introduced into BEAS-2B cells and retested using the variant testing platform. Consistent with the initial profiling data, *KRAS* variants showed greater *log*-fold resistance compared with vector control cells at higher radiation doses (**Fig. 7B**). In addition, there were evident intra-gene differences in the extent of resistance across domains (P-loop, Switch I, and Switch II), amino acid positions, and individual variants. For example, despite representing a confirmed oncogenic variant, D33E did not confer resistance at any dose of radiation (51). Overall, mutations within the switch II domain (e.g., Q61H and Q61L) were generally more likely to confer resistance (**Fig. 7B** and **C**). These results indicated that *KRAS* mutants confer cellular resistance to high-dose radiation with some intra-gene variant differences.

On the basis of these results, we posited that patients with *KRAS* mutant tumors are more likely to develop local treatment recurrence after high-dose thoracic radiation. To test this, we identified patients with primary lung cancer treated using high-dose radiation to the lung. We annotated cases for local failure outcomes, which we defined as radiographic progression within the irradiated volume (**Fig. 7D**). 85 patients from our cohort underwent *KRAS* genotyping; 33 patients had tumors with *KRAS* mutations (**Fig. 7E**). Patients with *KRAS* wild-type and mutant tumors had similar patient, tumor, and treatment characteristics (Supplementary Table S3). Critically, there were no significant differences in the two variates previously associated with local treatment failure in this setting: radiation dose delivered and tumor size (**Fig. 7F** and **G**; refs. 52, 53). Despite these similarities, patients with *KRAS* mutant tumors had a significantly higher rate of local treatment failure than those with *KRAS* wild-type tumors, with 3-year cumulative incidences of 31.7% (95% CI, 16.3–40.6) and 13.3% (95% CI, 5.3–25.1), respectively (**Fig. 7H**). A multivariate regression model that included *KRAS* gene status, tumor size, and radiation dose

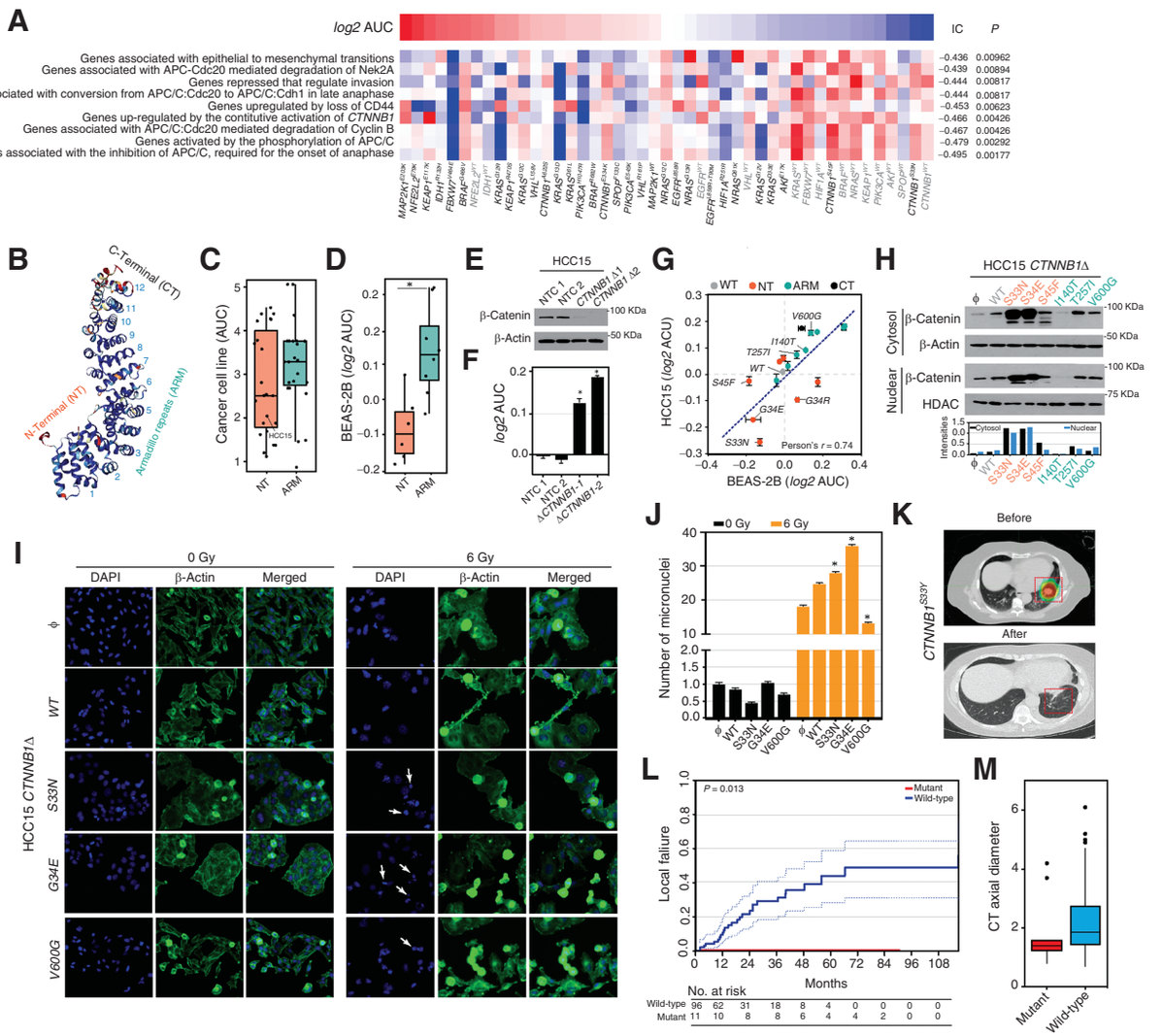

Figure 6.

CTNNB1 exon 3 variants confer radiation sensitivity via aberrant mitoses. **A,** ssGSEA identified gene sets associated with sensitivity to radiation. Heatmap of enrichment scores (red, positive; blue, negative). A subset of the top gene sets are shown. **B,** The crystal structure of wild-type CTNNB1 (PDB ID: 2z6h). Structural domains are shown. **C,** Cancer cell line radiation survival stratified by CTNNB1 domain. Tukey's boxplots [median and interquartile range (IQR)] are shown. **D,** 16 unique *CTNNB1* variants within the respective structural domains were assessed for radiation sensitivity in BEAS-2B cells. Tukey's boxplots (median and IQR) are shown. *, $P < 0.05$ by Welch *t* test. **E,** Immunoblot and (**F**) radiation survival of NTC or *CTNNB1*Δ HCC15 cells. *, $P < 0.05$ by Welch *t* test. **G,** Radiation survival, measured by *log*2 AUC values, for the designated variant-expressing cell lines were compared by scatterplot. Data are expressed as the means ± SEM. **H,** Immunoblots of a representative HCC15 *CTNNB1*Δ pooled clones expressing vector control (ϕ), wild-type *CTNNB1*, or the indicated variants. **I,** Fluorescence staining of the indicated *CTNNB1* variants expressed in HCC15 *CTNNB1*Δ cells. Arrows delimit micronuclei. **J,** Quantification of micronuclei, normalized to the vector control for each treatment arm (mock versus irradiated). *, $P < 0.05$ by Welch *t* test. **K,** Representative CT images of a patient with a *CTNNB1* mutant metastatic lung adenocarcinoma treated with high-dose thoracic radiation. Longitudinal CT image (*after*) demonstrates durable local control within the irradiated volume. **L,** Tukey's boxplots of the pre-therapy CT-derived maximum axial diameter of treated tumors stratified by *CTNNB1* genotype ($P = 0.21$; *t* test with Welch correction). **M,** Estimated cumulative incidence curves for local failure in the study population apportioned by *CTNNB1* genotype. Gray test was used to test for equality across the two groups.

showed that *KRAS* mutation status as the only variate that remained significant (Supplementary Table S4).

Because *KRAS* mutant tumors were resistant to radiation in cells and in patients, we posited that *KRAS* inhibitors may ameliorate treatment resistance. We tested a sequential treatment strategy with sotorasib, a small molecule that irreversibly inhibits $KRAS^{G12C}$, and radiation to optimize tumor control and potentially prevent treatment resistance. To assess the selectivity of the putative interaction between sotorasib and radiation, we profiled 3 lung adenocarcinoma PDX with *KRAS* wild-type, G12V, or G12C alleles (**Fig. 7I**). PDXs were passaged by single-step propagation into 20 mice representing 5 cohorts including mock (ϕ), sotorasib alone, radiation alone, sotorasib followed by radiation, and radiation followed by sotorasib. Radiation followed by sotorasib was the most effective sequence of therapy in the PDX driven by $KRAS^{G12C}$, indicating genotype and treatment sequence selective interactive tumor responses (**Fig. 7I**). These results indicated that

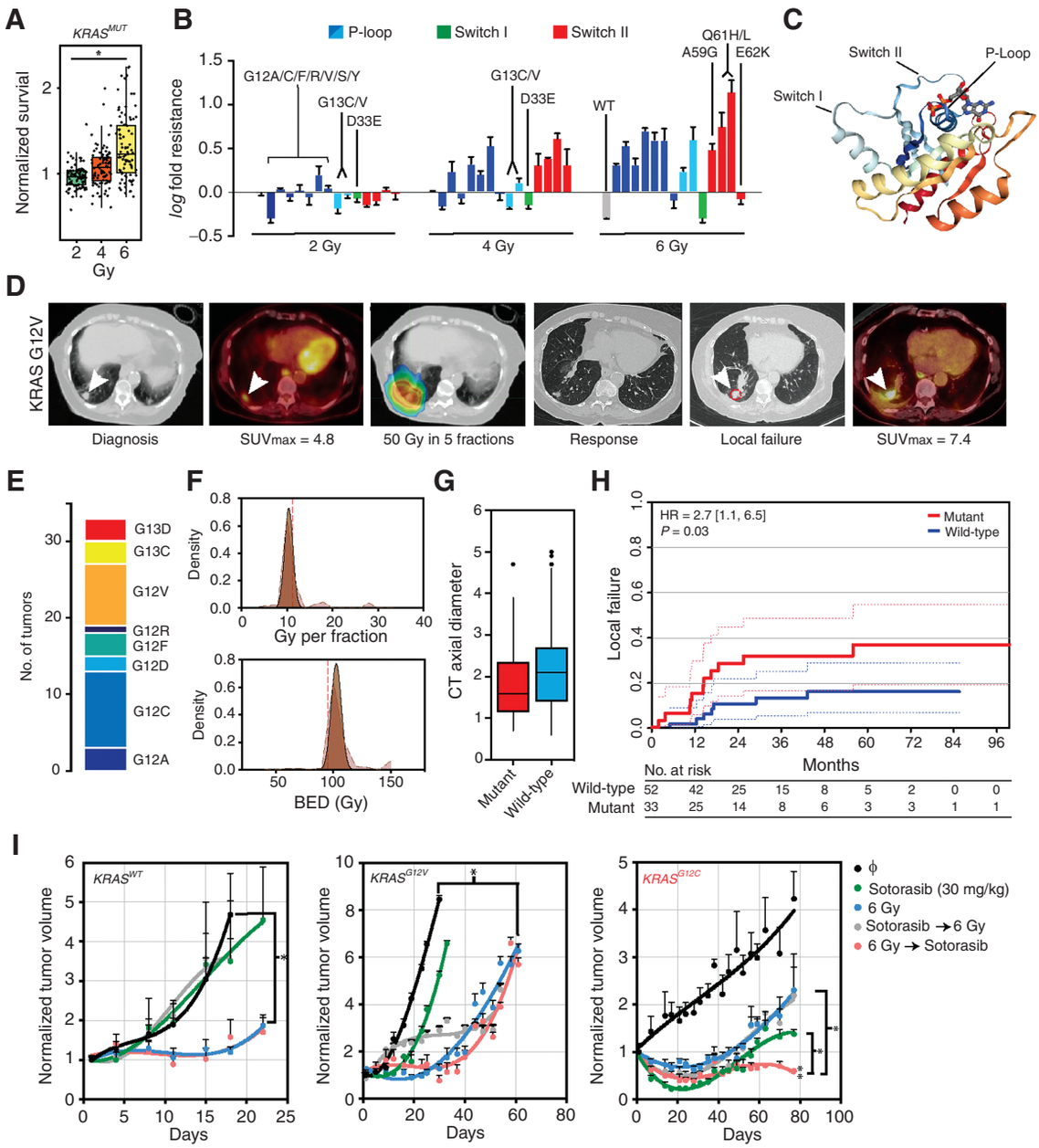

Figure 7.

KRAS variants confer resistance to high-dose radiation in cells, PDX, and patients. **A,** Normalized (to in plate vector control cells) survival of *KRAS* variant–expressing BEAS-2B cells at the indicated doses are displayed by Tukey's boxplots [median, interquartile range (IQR), and 1.5*x* of the IQR]. Individual points represent single biological replicate. **B,** 12 unique *KRAS* variants within the P-loop (blue), Switch I (green), or the Switch II (red) domain were retested for radiation resistance. The *y*-axis represents the *log*-fold change in survival compared with vector control treated cells at the indicated dose. Data bars represent mean ± SEM. **C,** The crystal structure of wild-type KRAS with GDP-bound is shown (PDB ID: 4obe). Selected structural regions with the most common hotspot mutations are highlighted: P-loop (residues 10–14), switch-I (residues 30–40), and switch-II (residues 58–72). **D,** Representative CT and PET/CT images of a patient with an early-stage *KRAS* mutant lung tumor treated with high-dose radiation. Serial CT images demonstrate treatment response followed by recurrence within the irradiated volume. Pretreatment and locally recurrent tumor PET/CT SUVmax values are shown. **E,** Stacked bar plot representing the number of individual *KRAS* variants in the clinical cohort ($n = 33$). **F,** Frequency distribution (light brown) and Gaussian fit for the fractional dose and the BED. Prescription radiation dose was adjusted for the number of fractions of radiation by calculating the biological effective dose (BED) with a standard α/β ratio of 10. **G,** Tukey's boxplots of the pre-therapy CT-derived maximum axial diameter of treated tumors stratified by *KRAS* genotype. **H,** Estimated cumulative incidence curves for local failure in the study population apportioned by *KRAS* genotype. Gray test was used to test for equality across the two groups. **I,** NSG mice bearing PDX with the indicated *KRAS* alleles in the flank were block randomized into one of five treatments arms. Sotorasib was given for 14 days every other day or as tolerated. Radiation was delivered in a single 6 Gy dose. Sequential treatments were given 24 to 48 hours after the completion of the first therapy. Data are expressed as the mean ± SEM; $n = 4$ independent animals for each arm. The *P* value of the χ^2 test between the indicated curves were deemed significant if < 0.05 (*). **, $P < 0.05$ for interaction based on two-way ANOVA.

adjuvant sotorasib treatment after high-dose radiation may ameliorate local treatment failures.

In the *KRAS*^{G12C} tumor, there was a lack of additivity or synergy in the sotorasib followed by radiation arm despite single-agent efficacy with drug and radiation alone. A mechanism that could explain the observed drug-radiation sequence dependence is rapid nonuniform adaptation after anti-Kras G12C drug. This adaptive mechanism has been shown to confer pathway reactivation after sustained inhibition using conformation dependent Kras G12C inhibitor (54). To assess whether the *KRAS*^{G12C}-driven tumor respresented in **Fig. 7I** was adapting to inhibition by sotorasib, we treated an *ex vivo* derivative of this tumor with drug for 24 and 72 hours followed by removal of the drug for 24 or 48 hours—the removal was intended to mimic the murine treatment schedule of a 24- to 48-hour break between drug and radiation. Lysates from these treatment conditions showed pathway reactivation after 72 hours of treatment (Supplementary Fig. S10). These results suggested that Kras activity can rapidly reemerge after sotorasib treatment, thus opposing the potential for additivity or synergy with combinatorial treatments.

Discussion

This study represents the largest analysis to date of the impact of gene mutations on radiation sensitivity. We profiled 396 unique SNVs across 92 genes using a previously benchmarked high-content irradiation platform (10). Our results provide new insights into the interplay between genetic features and radiation sensitivity and advance several principles that can guide theranostic and combinatorial strategies for patients receiving these treatments. We nominated variants for experimental profiling based on the radiation sensitivity data from a previously completed large-scale profiling effort (10). The nominated variants were significantly more likely to alter radiation sensitivity than those that were randomly selected or from CMGs that were not highly ranked by our association metrics. These results reinforce the importance of unbiased cellular profiling efforts in identifying new genetic determinants that are not merely associated with but also directly regulate radiation sensitivity.

We introduced gene variants into an immortalized upper airway lung epithelial cell line (BEAS-2B) with minimal underlying genomic alterations. In this manner, this cell line served as a *tabula rasa* for the introduction of variants culled from cancer genomes. This permitted the examination of variants without the potentially confounding influences of cancer genomic complexity. Despite these purported advantages, it is possible that the phenotypic output of some variants could be cellular context dependent. For example, variant activity could depend on the state of the signaling network within a cell and/or the tissue of origin (44). Our data, however, demonstrates that most impactful gene variants altered radiation sensitivity across oncogenic (i.e., immortalized and transformed cells) and tissue-delimited states. This supports the view that although cancer genomes reflect tissue-specific variant tendencies, genetic variants that alter radiation sensitivity can confer phenotypic effects across several cancer types.

Our results reveal critical differences between biomarkers for targeted drug therapeutics, which mainly adhere to a single gene-drug paradigm, and ionizing radiation. The genetic determinants of radiation sensitivity demonstrated significant locus heterogeneity, comprising a multitude of genes with roles in several cellular pathways that regulate the extent of cellular damage (e.g., enhanced reductive capacity) and/or the recovery from that damage after it is incurred (e.g., cell-cycle arrest and DNA repair). Integrative RNA and metabolite analyses suggested that although diverse at the origin, a multitude of variants converge on a few cellular pathways that ultimately alter radiation sensitivity. Despite this convergence, the interpretation of gene variants that alter radiation sensitivity as categorical variates, as is the case for targeted therapeutics, is imprecise and can obscure potentially actionable data. For example, we observed significant intra-gene variation in the magnitude of radiation sensitivity for both GOF and LOF variants. Genes like *KEAP1*, for example, which has been previously shown to confer resistance to radiation in clinical cohorts (55), demonstrated a near continuous effect size with no discernible hotspots, indicating that a comprehensive mutagenesis approach is likely to be required to adequately catalogue all functional variants (56). Moreover, oncogenes with significant mutational hot spots like *KRAS* and an established mechanistic role in regulating radiation resistance (57, 58) also had a range of activity across individual variants. Coupled with the ability to precisely adjust delivered doses of radiation, these results indicate that radiotherapeutic genomic biomarkers will be significantly more useful if they are both comprehensive and quantify the magnitude of the impact of individual mutations.

We validated some our findings using clinical cohorts that carefully annotated a radiotherapy specific outcome (i.e., local failure) rather than surrogates of treatment failures like progression-free survival or overall survival. Consistent with the functional data, we found that *CTNNB1* exon 3 and *KRAS* mutant tumors were associated significantly with local control and failure, respectively. In both cases, gene mutation status was the strongest predictor of local failure in a model that incorporated radiation dose and tumor volume. These results indicate that frequent (i.e., *KRAS*) and rare (i.e., *CTNBB1*) genetic features can be identified using our functional genomic tools. It remains unclear whether higher doses of radiation could potentially overcome *KRAS*-mediated treatment resistance because a generic radiation dose was delivered to most patients in our cohort. An alternative strategy supported by our PDX data suggests that KRAS G12C inhibitors may prevent local failures when delivered after radiotherapy. Moreover, our results suggest that dose de-escalation for *CTNNB1* exon 3 mutant tumors may be warranted. Both results set the stage for combinatorial therapeutic or prospective biomarker-stratified radiation dose modulation clinical studies, respectively.

Although we identified several genetic determinants that regulate the survival of cells after exposure to radiation, there are surely substantial additional variants. Many of the genes that we profiled were represented by relatively few variants and others were not represented. Although *in silico* prediction tools (13, 14) could aid in the characterization of these untested genes and variants, our results indicate that these tools alone are not sufficient to quantify categorical or continuous radiation sensitivity effects. Therefore, the bespoke functional genomic radiation platform presented herein coupled with iterative cycles of preclinical testing and clinical validation will be pivotal for refining clinical predictions. Lastly, although *KRAS/STK11* and *KEAP1/STK11* gene interactions represent a powerful initial assessment of the impact of co-altered genes on interactive radiation sensitivity, they are not comprehensive. Interrogating functionally relevant co-occurring genetic events will represent a critical step forward in the accurate prediction of clinical radiosensitivity.

In summary, our results reveal new insights into the mutational landscape of cancer's vulnerability to ionizing radiation. This information is poised to guide the transformation of radiotherapy from the current generic approach to one in which therapeutic strategies are guided by genetic alterations in individual patient tumors.

Authors' Disclosures

M.E. Abazeed reports grants from NIH during the conduct of the study; personal fees from American Society for Clinical Pathology, Mirati Therapeutics Inc.; and nonfinancial support from Siemens Healthineers outside the scope of the submitted work; in addition, M.E. Abazeed has a patent for compositions and methods for sensitizing a neoplastic cell to radiation issued, a patent for genospecific radiosensitization issued, a patent for decision support system for individualizing radiotherapy dose issued, and a patent for molecular predictors of patient response to radiotherapy treatment issued. No disclosures were reported by the other authors.

Authors' Contributions

P. Gopal: Conceptualization, resources, data curation, formal analysis, validation, investigation, visualization, methodology, writing–original draft, writing–review and editing. **B.D. Yard:** Conceptualization, resources, data curation, formal analysis, validation, investigation, methodology, writing–review and editing. **A. Petty:** Resources, data curation, investigation, methodology. **J.C. Lal:** Data curation, formal analysis, investigation, writing–review and editing. **T.K. Bera:** Resources, investigation, writing–review and editing. **T.Q. Hoang:** Resources, investigation. **A.D. Buhimschi:** Resources, validation, investigation, writing–review and editing. **M.E. Abazeed:** Conceptualization, resources, data curation, formal analysis, supervision, funding acquisition, visualization, methodology, writing–original draft, project administration, writing–review and editing.

Acknowledgments

M.E. Abazeed was supported by NIH R37CA222294 and P30CA060553. We thank the Northwestern University NUSeq and Metabolomics Cores for contributing to NGS and metabolite data, respectively.

The publication costs of this article were defrayed in part by the payment of publication fees. Therefore, and solely to indicate this fact, this article is hereby marked "advertisement" in accordance with 18 USC section 1734.

Note

Supplementary data for this article are available at Clinical Cancer Research Online (http://clincancerres.aacrjournals.org/).

Received June 15, 2022; revised August 24, 2022; accepted October 10, 2022; published first October 12, 2022.

References

1. Delaney G, Jacob S, Featherstone C, Barton M. The role of radiotherapy in cancer treatment: estimating optimal utilization from a review of evidence-based clinical guidelines. Cancer 2005;104:1129–37.
2. Hoadley KA, Yau C, Hinoue T, Wolf DM, Lazar AJ, Drill E, et al. Cell-of-origin patterns dominate the molecular classification of 10,000 tumors from 33 types of cancer. Cell 2018;173:291–304.
3. Marks LB, Yorke ED, Jackson A, Ten Haken RK, Constine LS, Eisbruch A, et al. Use of normal tissue complication probability models in the clinic. Int J Radiat Oncol Biol Phys 2010;76:S10–19.
4. Bergom C, West CM, Higginson DS, Abazeed ME, Arun B, Bentzen SM, et al. The implications of genetic testing on radiation therapy decisions: a guide for radiation oncologists. Int J Radiat Oncol Biol Phys 2019;105: 698–712.
5. Kerns SL, Fachal L, Dorling L, Barnett GC, Baran A, Peterson DR, et al. Radiogenomics Consortium Genome-Wide Association Study meta-analysis of late toxicity after prostate cancer radiotherapy. J Natl Cancer Inst 2020; 112:179–90.
6. Pitter KL, Casey DL, Lu YC, Hannum M, Zhang Z, Song X, et al. Pathogenic ATM mutations in cancer and a genetic basis for radiotherapeutic efficacy. J Natl Cancer Inst 2021;113:266–73.
7. Przybyla L, Gilbert LA. A new era in functional genomics screens. Nat Rev Genet 2022;23:89–103.
8. Bardelle C, Boros J. Development of a high-content high-throughput screening assay for the discovery of ATM signaling inhibitors. J Biomol Screen 2012;17: 912–20.
9. Tseng H-M, Shum D, Bhinder B, Escobar S, Veomett NJ, Tomkinson AE, et al. A high-throughput scintillation proximity-based assay for human DNA ligase IV. Assay Drug Dev Technol 2012;10:235–49.
10. Yard BD, Adams DJ, Chie EK, Tamayo P, Battaglia JS, Gopal P, et al. A genetic basis for the variation in the vulnerability of cancer to DNA damage. Nat Commun 2016;7:11428.
11. Lawrence MS, Stojanov P, Polak P, Kryukov GV, Cibulskis K, Sivachenko A, et al. Mutational heterogeneity in cancer and the search for new cancer-associated genes. Nature 2013;499:214–8.
12. Gopal P, Sarihan EI, Chie EK, Kuzmishin G, Doken S, Pennell NA, et al. Clonal selection confers distinct evolutionary trajectories in BRAF-driven cancers. Nat Commun 2019;10:5143.
13. Chang MT, Bhattarai TS, Schram AM, Bielski CM, Donoghue MTA, Jonsson P, et al. Accelerating discovery of functional mutant alleles in cancer. Cancer Discov 2018;8:174–83.
14. Gao J, Chang MT, Johnsen HC, Gao SP, Sylvester BE, Sumer SO, et al. 3D clusters of somatic mutations in cancer reveal numerous rare mutations as functional targets. Genome Med 2017;9:4.
15. Berger AH, Brooks AN, Wu X, Shrestha Y, Chouinard C, Piccioni F, et al. High-throughput phenotyping of lung cancer somatic mutations. Cancer Cell 2016;30: 214–28.
16. Giacomelli AO, Yang X, Lintner RE, McFarland JM, Duby M, Kim J, et al. Mutational processes shape the landscape of TP53 mutations in human cancer. Nat Genet 2018;50:1381–7.
17. Ursu O, Neal JT, Shea E, Thakore PI, Jerby-Arnon L, Nguyen L, et al. Massively parallel phenotyping of coding variants in cancer with Perturb-seq. Nat Biotechnol 2022;40:896–905.
18. Boucher JI, Bolon DN, Tawfik DS. Quantifying and understanding the fitness effects of protein mutations: Laboratory versus nature. Protein Sci 2016;25: 1219–26.
19. Gong LI, Suchard MA, Bloom JD. Stability-mediated epistasis constrains the evolution of an influenza protein. Elife 2013;2:e00631.
20. Abazeed ME, Adams DJ, Hurov KE, Tamayo P, Creighton CJ, Sonkin D, et al. Integrative radiogenomic profiling of squamous cell lung cancer. Cancer Res 2013;73:6289–98.
21. Zheng S, Wang W, Aldahdooh J, Malyutina A, Shadbahr T, Tanoli Z, et al. SynergyFinder Plus: Toward better interpretation and annotation of drug combination screening datasets. Genomics Proteomics Bioinformatics 2022: S1672-0229(22)00008-0.
22. Barretina J, Caponigro G, Stransky N, Venkatesan K, Margolin AA, Kim S, et al. The Cancer Cell Line Encyclopedia enables predictive modelling of anticancer drug sensitivity. Nature 2012;483:603–7.
23. Dobin A, Davis CA, Schlesinger F, Drenkow J, Zaleski C, Jha S, et al. STAR: ultrafast universal RNA-seq aligner. Bioinformatics 2013;29:15–21.
24. Pons C, Almacellas E, Tauler A, Mauvezin C. Detection of Nuclear Biomarkers for Chromosomal Instability. In: Norberg H, Norberg E, editors. Autophagy and cancer: methods and protocols. New York: Springer US; 2022. p. 117–25.
25. Vargas R, Gopal P, Kuzmishin GB, DeBernardo R, Koyfman SA, Jha BK, et al. Case study: patient-derived clear cell adenocarcinoma xenograft model longitudinally predicts treatment response. NPJ Precis Oncol 2018;2:14.
26. Timmerman RD, Hu C, Michalski J, Straube W, Galvin J, Johnstone D, et al. Long-term results of RTOG 0236: a phase II trial of stereotactic body radiation therapy (SBRT) in the treatment of patients with medically inoperable stage I non–small cell lung cancer. Int J Radiat Oncol Biol Phys 2018;4:1287–8.
27. Scrucca L, Santucci A, Aversa F. Regression modeling of competing risk using R: an in depth guide for clinicians. Bone Marrow Transplant 2010;45:1388–95.
28. TeamR R: A Language and Environment for Statistical Computing. Vienna, Austria: R Foundation for Statistical Computing; 2013.
29. Cover TM, Thomas JA. Elements of Information Theory (Wiley Series in Telecommunications and Signal Processing). New Jersey: Wiley-Interscience; 2006.
30. UniProt C. UniProt: the universal protein knowledgebase in 2021. Nucleic Acids Res 2021;49:D480–9.
31. Gao J, Aksoy BA, Dogrusoz U, Dresdner G, Gross B, Sumer SO, et al. Integrative analysis of complex cancer genomics and clinical profiles using the cBioPortal. Sci Signal 2013;6:pl1.

32. Reddel RR, Ke Y, Gerwin BI, McMenamin MG, Lechner JF, Su RT, et al. Transformation of human bronchial epithelial cells by infection with SV40 or adenovirus-12 SV40 hybrid virus, or transfection via strontium phosphate coprecipitation with a plasmid containing SV40 early region genes. Cancer Res 1988;48:1904–9.
33. Cuella-Martin R, Oliveira C, Lockstone HE, Snellenberg S, Grolmusova N, Chapman JR. 53BP1 Integrates DNA repair and p53-dependent cell fate decisions via distinct mechanisms. Mol Cell 2016;64:51–64.
34. Goncearenco A, Rager SL, Li M, Sang QX, Rogozin IB, Panchenko AR. Exploring background mutational processes to decipher cancer genetic heterogeneity. Nucleic Acids Res 2017;45:W514–22.
35. Chakravarty D, Gao J, Phillips SM, Kundra R, Zhang H, Wang J, et al. OncoKB: A precision oncology knowledge base. JCO Precis Oncol 2017;2017:PO.17.00011.
36. Brown AL, Li M, Goncearenco A, Panchenko AR. Finding driver mutations in cancer: elucidating the role of background mutational processes. PLoS Comput Biol 2019;15:e1006981.
37. Gonzalez F, Zhu Z, Shi Z-D, Lelli K, Verma N, Li QV, et al. An iCRISPR platform for rapid, multiplexable, and inducible genome editing in human pluripotent stem cells. Cell Stem Cell 2014;15:215–26.
38. Larson MH, Gilbert LA, Wang X, Lim WA, Weissman JS, Qi LS. CRISPR interference (CRISPRi) for sequence-specific control of gene expression. Nat Protoc 2013;8:2180–96.
39. Garcia-Tunon I, Alonso-Perez V, Vuelta E, Pérez-Ramos S, Herrero M, Méndez L, et al. Splice donor site sgRNAs enhance CRISPR/Cas9-mediated knockout efficiency. PLoS One 2019;14:e0216674.
40. Hast BE, Cloer EW, Goldfarb D, Li H, Siesser PF, Yan F, et al. Cancer-derived mutations in KEAP1 impair NRF2 degradation but not ubiquitination. Cancer Res 2014;74:808–17.
41. Ohta T, Iijima K, Miyamoto M, Nakahara I, Tanaka H, Ohtsuji M, et al. Loss of Keap1 function activates Nrf2 and provides advantages for lung cancer cell growth. Cancer Res 2008;68:1303–9.
42. Panier S, Boulton SJ. Double-strand break repair: 53BP1 comes into focus. Nat Rev Mol Cell Biol 2014;15:7–18.
43. Schaefer MH, Serrano L. Cell type–specific properties and environment shape tissue specificity of cancer genes. Sci Rep 2016;6:20707.
44. Poulin EJ, Bera AK, Lu J, Lin Y-J, Strasser SD, Paulo JA, et al. Tissue-specific oncogenic activity of KRAS(A146T). Cancer Discov 2019;9:738–55.
45. Ji H, Ramsey MR, Hayes DN, Fan C, McNamara K, Kozlowski P, et al. LKB1 modulates lung cancer differentiation and metastasis. Nature 2007;448:807–10.
46. Cancer Genome Atlas Research N. Comprehensive molecular profiling of lung adenocarcinoma. Nature 2014;511:543–50.
47. Lieu EL, Nguyen T, Rhyne S, Kim J. Amino acids in cancer. Exp Mol Med 2020;52:15–30.
48. Tardito S, Oudin A, Ahmed SU, Fack F, Keunen O, Zheng L, et al. Glutamine synthetase activity fuels nucleotide biosynthesis and supports growth of glutamine-restricted glioblastoma. Nat Cell Biol 2015;17:1556–68.
49. Dixon SJ, Patel DN, Welsch M, Skouta R, Lee ED, Hayano M, et al. Pharmacological inhibition of cystine-glutamate exchange induces endoplasmic reticulum stress and ferroptosis. Elife 2014;3:e02523.
50. Gao C, Wang Y, Broaddus R, Sun L, Xue F, Zhang W. Exon 3 mutations of CTNNB1 drive tumorigenesis: a review. Oncotarget 2018;9:5492–508.
51. Kim E, Ilic N, Shrestha Y, Zou L, Kamburov A, Zhu C, et al. Systematic functional interrogation of rare cancer variants identifies oncogenic alleles. Cancer Discov 2016;6:714–26.
52. Dunlap NE, Larner JM, Read PW, Kozower BD, Lau CL, Sheng K., et al. Size matters: a comparison of T1 and T2 peripheral non–small cell lung cancers treated with stereotactic body radiation therapy (SBRT). J Thorac Cardiovasc Surg 2010;140:583–9.
53. Kestin L, Grills I, Guckenberger M, Belderbos J, Hope AJ, Werner-Wasik M, et al. Dose-response relationship with clinical outcome for lung stereotactic body radiotherapy (SBRT) delivered via online image guidance. Radiother Oncol 2014;110:499–504.
54. Xue JY, Zhao Y, Aronowitz J, Mai TT, Vides A, Qeriqi B, et al. Rapid nonuniform adaptation to conformation-specific KRAS(G12C) inhibition. Nature 2020;577:421–5.
55. Binkley MS, Jeon Y-J, Nesselbush M, Moding EJ, Nabet BY, Almanza D, et al. KEAP1/NFE2L2 mutations predict lung cancer radiation resistance that can be targeted by glutaminase inhibition. Cancer Discov 2020;10:1826–41.
56. Zheng L, Baumann U, Reymond JL. An efficient one-step site-directed and site-saturation mutagenesis protocol. Nucleic Acids Res 2004;32:e115.
57. Yang L, Shen C, Estrada-Bernal A, Robb R, Chatterjee M, Sebastian N, et al. Oncogenic KRAS drives radioresistance through upregulation of NRF2–53BP1-mediated nonhomologous end-joining repair. Nucleic Acids Res 2021;49:11067–82.
58. Wang M, Han J, Marcar L, Black J, Liu Q, Li X, et al. Radiation resistance in KRAS-mutated lung cancer is enabled by stem-like properties mediated by an Osteopontin–EGFR pathway. Cancer Res 2017;77:2018–28.